



On the kinetics of photoelectrocatalytic water splitting on nanocrystalline TiO₂ films

Andreas K. Seferlis, Stylianos G. Neophytides*

Foundation of Research and Technology Hellas, Institute of Chemical Engineering Sciences (FORTH/ICE-HT), Platani, GR26504 Rion Patras, Greece

ARTICLE INFO

Article history:

Received 4 August 2012

Received in revised form

10 December 2012

Accepted 13 December 2012

Available online 21 December 2012

Keywords:

Photo electrocatalysis

Water splitting

Wet electron state

TiO₂ nanocrystalline film

ABSTRACT

Water splitting photoelectrocatalytic reaction mechanism on TiO₂ nano particulate polycrystalline film has been studied by means of potentiostatic and potentiodynamic measurements in alkaline solutions under UV irradiation peaking at 365 nm. The TiO₂ photoelectrode is reduced by scanning to negative potentials and its photoelectrocatalytic activity is enhanced. This is attributed to the formation of defect states within the bandgap created while in negative potential. The defect states can be responsible for the appearance of the two kinetic regions observed in the potentiostatic experiments. These are located within the potential range -0.1 to 0.3 V (region I) and 0.3 – 0.8 V (region II) vs. RHE, respectively, and can be activated by different states positioned at different energy levels within the bandgap of TiO₂. For film thickness <5 μm region I does not appear and the open circuit voltage (OCV) shifts to more positive values by 0.35 V as compared to thicker electrodes. The splitting of adsorbed water can be realized through the activation of the ‘wet electron’ state of adsorbed water molecules, which is activated by photo-excited electrons originating from bandgap states positioned closer to the bottom of the conduction band. Based on the OH_{ad} reduction peak of the cyclic voltammograms (CV) and the BET surface area of the ~ 5 μm thick TiO₂ electrode, the electrochemical utilization of TiO₂ film specific surface area was found to be 100% and the maximum turn over frequency at the saturation photocurrent 0.7 s^{−1}.

© 2012 Elsevier B.V. All rights reserved.

1. Introduction

Solar energy conversion and storage is a long sought goal for the scientific community. This goal can be achieved by the photoelectrolysis of water on semiconductor/electrolyte interfaces. Those materials act as the light absorbers and convert solar energy into chemical energy that is stored in H₂ [1]. One of the most promising and widespread semiconducting materials in photocatalysis and photoelectrocatalysis is Titanium oxide (Titania, TiO₂) either as a photoactive catalyst support or as photoanode in photoelectrochemical cells (PEC). In the latter particularly TiO₂ is used as photoelectrode in dye sensitized solar cells (DSSC) [2], as photoanode in PEC for water splitting [3–6] and photoelectroreforming of organic compounds [7,8]. TiO₂ is remarkably stable as a photoactive material but its main drawback is the wide band gap (3.2 eV for anatase), which limits its photoexcitation under illumination to UV light. In its stoichiometric form is an inert wide bandgap insulator, while upon partial reduction its photoelectrochemical properties are being enhanced due to formation of defect states that are being located within the bandgap just below the bottom of the conduction band [9]. Recent experimental and theoretical studies [9–11]

dealt with the investigation and understanding of the TiO₂ surface and bulk chemistry of these defect states and their interaction with H₂, O₂ and H₂O molecules [10,12,13]. In general the partial reduction of TiO₂ and formation of defect states is substantiated through the charge distribution in the bulk (Ti interstitials) and on surface Ti sites [14]. These defect states provide the surface charge for the interactions of the aforementioned molecules with the surface, while they can be effectively photoexcited to provide electrons to the conduction band.

Despite the vast literature for the photoelectrochemical properties of TiO₂ there is still lack of understanding with regards to the nature of the photoelectrocatalytically active surface sites, the photoelectrochemical interfacial reactions for water splitting on the TiO₂ surface and the surface chemistry of the TiO₂ photoanode during the course of the photo(electro)excitation process. According to the established realization of the photoexcitation process the general reaction scheme involves the exciton formation and its reaction with the adsorbed reacting species or molecules. In this respect according to reaction scheme (1)–(3) the positive holes (h^+) formed upon illumination (reaction (1)) are considered as the active site on the photo anode's surface (reaction (2)) the nature of which is not substantially defined.



* Corresponding author. Tel.: +30 2610965265; fax: +30 2610965223.

E-mail address: neoph@iceht.forth.gr (S.G. Neophytides).

Table 1
Deposited TiO₂ amounts and film thickness.

Sample	Film thickness (μm)	TiO ₂ amount (μg/cm ²)
A	3.27	1.07
B	4.97	1.91
C	15.5	6.22



In the case of TiO₂ it can be said that a general acceptance dominates that considers the oxygen vacancies on its surface to coincide with the positive hole formation implying that TiO₂ surface is partially reduced upon irradiation.

In general three types of active sites can be distinguished on a TiO₂ surface: the pentacoordinated Ti atoms, the O_{br} vacancies and the O_{br} atoms. As it has been established by several studies all reacting molecules initially interact and adsorb on the pentacoordinated surface terminal Ti atoms. Thereafter the adsorbed species may react with the neighboring O_{br} vacancy or with neighboring O_{br} atom [15–18]. In the case of water adsorption a dynamic equilibrium is established between the adsorbed water molecule and bridged hydroxyl species, OH_{br}, or hydroxyl adsorbed on top of the terminal Ti atoms, OH_t [19]. This is facilitated through the formation of hydrogen bonds and the perpetual transfer of hydrogen atoms between adjacent O_{br} and adsorbed O_t on terminal Ti [13].

The exact mechanism and electrokinetics of photoelectrochemical water splitting on TiO₂ is mostly not well understood as of the nature of the active sites and the surface species involved in the photoelectrochemical process. In particular two surface reaction mechanisms have been proposed in order to interpret the interaction of H₂O with the photoexcited TiO₂ surface. Salvador [18] has proposed the Redox Photooxidation (RP) mechanism according to which photooxidation of water species is initiated by inelastic interfacial transfer of free valence band (VB) photogenerated holes to filled bandgap states associated with OH_{ads}[−]/(H₂O)_{ads} TiO₂ adsorbed water species, giving rise to OH_s[•] radicals which thereafter react to form H₂O₂. Nakato and co-workers [17] proposed the nucleophilic attack (NA) mechanism as an alternative acid–base water photooxidation. Water molecule (Lewis base) reacts with a surface trapped hole (Lewis acid) on an O_{br} site, followed by Ti–O bond breaking.

In the present study, based on potentiodynamic and potentiostatic measurements of TiO₂ photoanode immersed in an alkaline electrolyte, we are discussing the photoelectrocatalytic reaction mechanism for water splitting in the light of a novel approach regarding the formation and the role of the defect states on the photo excitation properties of TiO₂. Water splitting is being realized through the activation of the TiO₂ surface ‘wet electron’ state [9] within the adsorbed clusters of the water molecules by the photoexcited electrons originating from the TiO₂ bandgap defect states.

In this respect we will try to discuss and introduce the ‘wet electron’ state idea as the principle mechanism that governs the kinetics of the photoelectrochemical water splitting [19]. The ‘wet electron’ state can be substantiated within the monolayer of the adsorbed water molecules and the dangling H atoms on top of the O_{br} species and was explicitly studied by Onda et al. [9] by means of Time Resolved two Photon Photoemission (TR-2PP) electron spectroscopy [9,11,19]. At approximately one monolayer coverage of water on partially hydroxylated TiO₂ surfaces, they found an unoccupied electronic state 2.4 eV above the Fermi level. The unoccupied ‘wet electron’ state can be filled by photoexcited electrons mostly originating from the defect states in the bandgap. Though it is believed that the ‘wet electron’ may play the prime

role in electrochemical and photo electrochemical charge transfer reactions, its role is not yet evident.

2. Experimental

2.1. Electrode preparation

All chemicals were purchased from Aldrich and were used without any further purification. Water from a Millipore installation was used in all experimental procedures.

Titania films were deposited on indium–tin oxide coated glass slides with 8–12 Ω/sq initial surface resistivity via dip-coating method [20]. A solution containing 10.5 g Triton X-100, 10.2 ml acetic acid, 57 ml pure ethanol and 5.4 ml titanium tetraisopropoxide was kept under vigorous stirring. ITO glass slides were cleaned with ethanol and distilled water and calcinated at 550 °C. Afterwards they were immersed in the solution, so that 5.5 cm of the long side of the slide was wetted by the sol, and abruptly withdrawn. The back-side (non conductive) of the slide was carefully swept dry and the slide was calcinated at 550 °C for 15 min with a heating/cooling rate of 15 °C/min. The whole procedure was repeated, as required, until the desired amount of titania was deposited on the slide. The electrodes were transparent except for samples subjected to more than approx. 15 cycles of dip-coating that gradually became white. As shown in Table 1 three samples were prepared and tested within the framework of the present study. The samples were prepared with varying film thickness and TiO₂ amount in order to study the effect of film thickness on the efficiency of the photoelectrochemical process.

2.2. Electrode characterization

The morphology and structural characteristics of the electrodes was investigated by scanning electron microscopy (SEM, LEO SUPRA 35VP), X-ray diffraction (XRD, Bruker D8 advance XRD) with the following characteristics: CuKα, λ = 1.5406 Å, 40 kV, 40 mA and 2θ ranging 20–70°, and the BET specific surface area was measured by N₂ physisorption by the use of a Quantachrome Autosorb-1.

2.3. Experimental setup

The photoelectrochemical reactor used in all experiments was a Plexiglas cylindrical cell described in detail in references [7,21]. A Philips lamp (TL4W/08 blb F8T5) was vertically positioned in the center of the reactor. The lamp emits light mainly in the ultraviolet region with a peak at 365 nm. The incident power density of the lamp was measured 0.72 mW/cm². The schematic diagram of the cell and the flow system is shown in Fig. 1. The cell and the flow system were designed so that the evolved gas (O₂) from the photoanode was separated by the gas evolved (H₂) at the cathode counter electrode. The He introduced in the two compartments (1 and 2 in Fig. 1) was used as a carrier gas and a needle valve (9 Fig. 1) was placed at the cathode flow stream (1 in Fig. 1) in order to equilibrate the pressure in the two compartments, thus being able to avoid electrolyte's overflow. The gas analysis was carried out by means of online gas chromatography (GC) by the use of a six port valve to a Varian GC, model CP 3380 equipped with a Carbosieve S-II column. All voltage values in the text are recorded vs. reference hydrogen electrode (RHE).

The ITO substrate with the deposited TiO₂ film was placed in the photo electrochemical cell so that it is irradiated from the front side of the film that is interfacing the electrolyte. The surface area of the film immersed in the electrolyte is 13.75 cm². The electrolyte's concentration was set at 0.1 M NaOH. All electrochemical

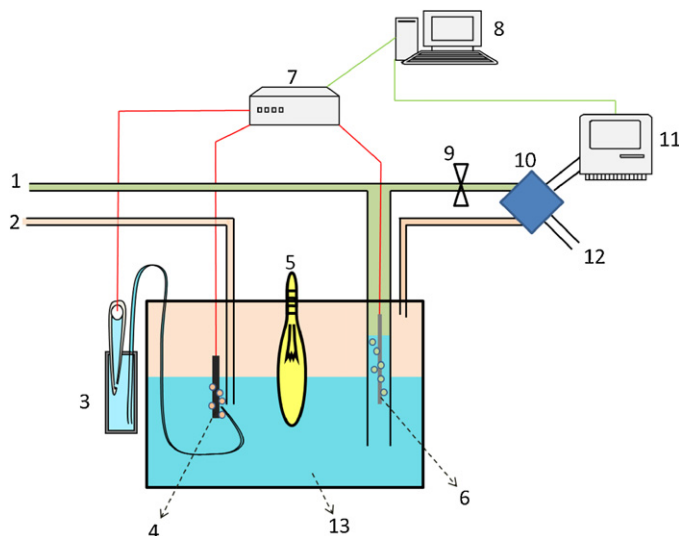


Fig. 1. Reactor and gas flow system schematic representation. (1) Counter electrode Helium gas flow, (2) main chamber Helium gas flow, (3) reference electrode with Luggin capillary, (4) working TiO₂ photoelectrode, (5) UV lamp, (6) counter electrode with hydrogen bubbles, (7) potentiostat, (8) PC, (9) needle valve for pressure drop equilibration between the inlet flows 1 and 2, (10) 4-way valve, (11) gas chromatographer, (12) vent, and (13) electrolyte

measurements (steady state *I*–*V* plots, and cyclic voltammetry) were carried out using a PAR 263A potentiostat.

2.3.1. Photo electrode's efficiencies

The quantum yield in photoelectrochemical systems is expressed by the Incident Photon to Charge carrier Efficiency (IPCE%) and is represented by Eq. (4):

$$\text{IPCE}\% = \frac{1240 \times J(\text{mA}/\text{cm}^2)}{\lambda(\text{nm}) \times P(\text{mW}/\text{cm}^2)} \times 100 \quad (4)$$

J corresponds to the current density of the electrochemical current driven through the photoanode/electrolyte interface, λ is the wave length (365 nm) of the incident radiation and *P* is the incident's radiation power density (0.72 mW/cm²) at the electrode's surface. At IPCE = 100% one incident photon corresponds to one excited electron, which is successfully collected at the external circuit.

An alternative useful definition measures the Gibbs free energy efficiency, η_G , which is defined as the ratio of the maximum electrical power that can be derived from the chemical generated in the cell to the solar irradiance [22]:

$$\eta = \frac{\Delta G^\circ r_p}{P_T} \quad (5)$$

where r_p is the rate of formation of product *p* e.g. H₂ (mol s^{−1}) per unit area of the photoelectrode and ΔG° is the standard Gibbs energy generated by this product in an ideal fuel cell (J mol^{−1}). When an external bias (*V*_{bias}) is applied between the two electrodes to assist the cell reaction, its contribution should be taken into account and Eq. (5) is written as

$$\eta = \frac{\Delta G^\circ r_p - V_{\text{bias}} i_p}{P_T} \quad (6)$$

where i_p is the current responsible for the generation of product *p* at the rate of r_p .

3. Results

3.1. Electrode morphology and physicochemical characterization

The morphology of the TiO₂ samples is similar to the SEM images reported in reference [21]. The film thickness of TiO₂ depends on the number of dip-coating cycles and varied between 3 μm and 15 μm (Table 1). A cracked-mud morphology was obtained that can be attributed to shrinkage upon drying [23]. However no significant difference in the morphology of the samples between successive dip-coating cycles was noted. The structure of the samples is uniform and consists of grains with diameter ranging between 20 and 25 nm through out the bulk of the film. This result is in good accordance with the XRD spectra not shown here for brevity. The samples were exclusively anatase phase. According to Scherrer equation a particle size of 15 nm was calculated. The BET surface area of the samples was measured ca. 20 m²/g, which corresponds to an average particle size of 35 nm. Thus based on the amount of the deposited TiO₂, the roughness factor of the nanocrystalline films varies between 257 and 1257 for film thickness between 3 and 15 μm respectively. The high roughness factor in combination with the nanosized particle size is expected to provide a highly efficient photo-electrochemical interface.

3.2. Photoelectrochemical properties of TiO₂ electrode

When a titania electrode was employed in 0.1 M NaOH in dark, the open circuit voltage (OCV), after degassing with Helium, ranged between 0.6 V and 0.8 V. Under illumination, the OCV dropped within the range of −80 to 200 mV vs. a RHE. As it will be discussed further on, the exact value of the OCV was dependent on the film thickness.

In order to investigate the electrode's response to light and clarify the nature of the photo induced active sites as well as the species involved in the electrocatalytic reactions at the interface, we employed cyclic voltammetry under various conditions both in dark and under illumination. The results are shown in Fig. 2, where the cyclic voltammograms (CVs) under dark and under irradiation conditions are depicted. The lower limit of the scans was set at −0.4 V, as preliminary experiments showed that the titania electrode deteriorates at lower potentials, most probably due to extensive reduction and loss of its semiconducting features.

At approximately 0.1 V a reduction peak is observed during the cathodic scan. At more negative potentials the increased negative current is expected to induce higher degree of reduction of the TiO₂ surface. Its corresponding reoxidation appears during the subsequent anodic scan with the evolution of the anodic peak at −0.15 V. Thereafter an oxidation peak appears at 0.2 V, which can be enhanced after several days of operation (Fig. 2b). Although this peak is located opposite to the reduction peak at 0.1 V, it will be shown that the two peaks do not correspond to the same redox electrochemical process. In the region above 0.4 V and up to 1.4 V no significant current is observed in dark, indicating that TiO₂ is electrocatalytically inactive. Under illumination, an anodic photocurrent is observed that increases with applied potential at values more positive than 0.4 V, reaching a plateau above 0.8 V. The saturation/limiting photo current corresponds to the highest electron–hole separation due to the depletion of electrons in the space charge region upon withdrawal of electrons to the external circuit [12].

As it is clearly observed, the irradiation of the electrode induces the significant enhancement of the reduction peak at 0.1 V (Fig. 2a). The anodic peak at 0.2 V is enhanced too, though not at the same degree as in the case of the reduction peak at 0.1 V. It must be noted that the current in the region at the lower negative limit of the CV (−0.4 V) is essentially the same, reaching the same values both

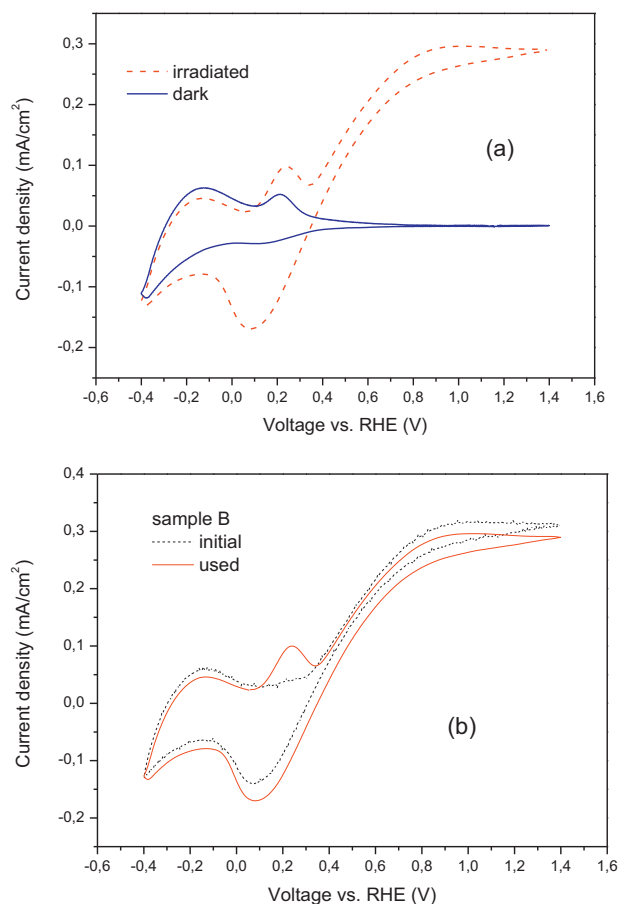


Fig. 2. Characteristic CV in dark and under irradiation. (a) Cyclic voltammogram in dark (blue solid line) and under illumination (red dashed line). Scan rate 5 mV/s. (b) Cyclic voltammograms: initial (black dotted line) and used (red solid line). Scan rate 5 mV/s. Sample B see Table 1. (For interpretation of the references to color in this figure legend, the reader is referred to the web version of the article.)

under dark and under illumination. It is also interesting to notice that at -0.15 V oxidation anodic peak is, in both cases under dark and under illumination, very similar in shape and size.

Fig. 3a depicts the transient evolution of the cyclic voltammograms under illumination. As it is interestingly observed the saturation photocurrent increases upon successive potential cycling. During the second scan the saturation photocurrent increases by 40% and stabilizes to the final value which is 60% higher than the initial scan. However, as depicted in Fig. 3b, when the cathodic scan limit is set at less negative potential (-200 mV) the saturation photocurrent reaches less than half of the photocurrent value observed in the cyclic voltammograms of Fig. 3a. This behavior strongly indicates that the electrochemical reduction of the TiO_2 surface during the cathodic scan is affecting the photoelectrocatalytic activity of the TiO_2 film.

Fig. 4 shows the photoelectrochemical response of the TiO_2 surface under He, H_2 and O_2 bubbling. As it is shown the reduction peak at 0.1 V has been almost eliminated when H_2 is being bubbled through the solution. This strongly indicates that the adsorbed oxidic species, most probably OH_{ad} adsorbed on Ti terminal atoms (see Section 4), being formed during the anodic scan, directly react with and are reduced by H_2 , instead of being reduced by the cathodic current. By calculating the difference in the area between the recorded peak under He and H_2 we can estimate the OH_{ad} coverage that is adsorbed on the surface of the TiO_2 photoelectrode. Based on the measured BET surface area of the nanocrystalline TiO_2 electrode, $20 \text{ m}^2/\text{g}$, it is estimated that $0.9 \times 10^{15} \text{ OH}_{\text{ad}}$ species/cm² are

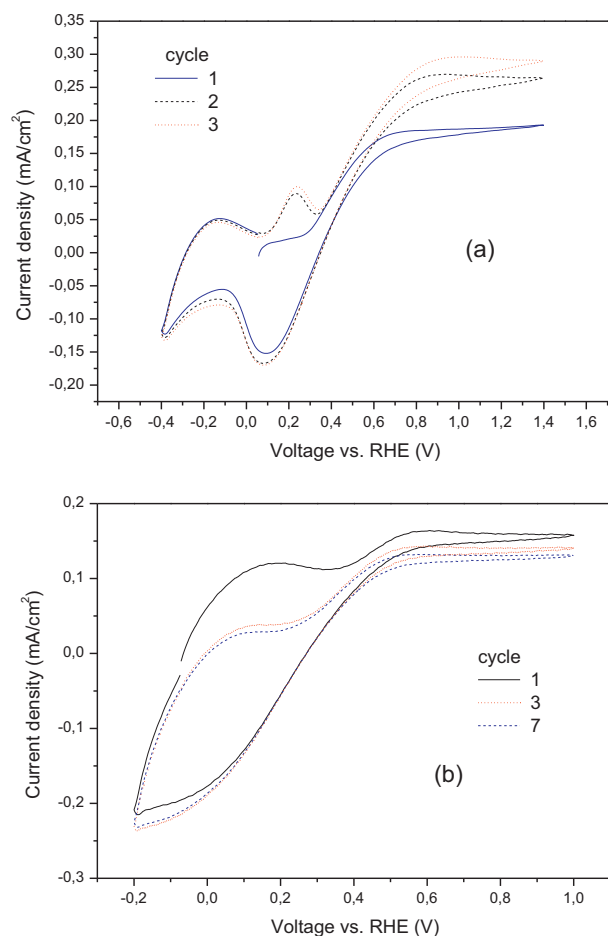


Fig. 3. Dynamic evolution of cyclic voltammograms. (a) Cycling limits (-0.4) to (1.4) V, scan rate is 5 mV/s. (b) cycling limits (-0.2) to (1.0) V, scan rate is 50 mV/s. Sample B see Table 1.

adsorbed, which is more than twice the number of pentacoordinated terminal Ti atoms ($0.4 \times 10^{15} \text{ Ti atoms/cm}^2$) on a rutile (1 1 0) plane [10]. The double coverage estimated for the OH_{ad} species can be attributed to the fact that the TiO_2 film is anatase, which mainly contains pentacoordinated terminal Ti atoms [24]. Though molecular H_2 may react with the adsorbed oxidic species on the

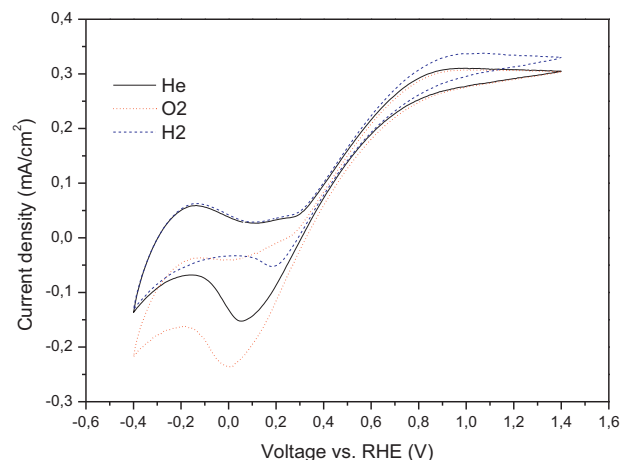


Fig. 4. Cyclic voltammograms under various gas atmospheres. Helium (black solid line), Oxygen (dashed-dotted red line), and Hydrogen (dotted blue line) atmospheres. Scan rate 50 mV/s. Sample B see Table 1. (For interpretation of the references to color in this figure legend, the reader is referred to the web version of the article.)

TiO₂ surface, this is not the case of molecular H₂ interaction with the electrochemically reduced TiO₂ surface. This can be deduced by the CV depicted in Fig. 4, which shows that under H₂ bubbling the anodic oxidation peak at -0.15 V remains unaffected as compared to the corresponding peak under He atmosphere. Such behavior suggests that this anodic oxidation peak is not related to the oxidation of any adsorbed H_{ad} species but instead to the reduction/oxidation of the surface by the removal of O species most probably O_{br} (bridged oxygen). This is corroborated by the observation that during O₂ bubbling, the anodic peak at -0.15 V has been almost diminished, most probably due to the fast replacement of the abstracted O_{br} by the supplied gas phase oxygen.

It is noticeable that during O₂ bubbling the whole CV spectrum below 0.4 V is shifted to negative currents, as compared to the spectrum under He flow. The shift of the spectrum toward negative currents shows that O₂ interacts electrocatalytically with the reduced TiO₂ surface and most probably on sites that are being created during the cathodic scan. On the contrary a minor effect on the photocurrent is observed during H₂ bubbling. Though H₂ reacts with the formed OH_{ad} species its contribution in the enhancement of saturation photocurrent is minimal and confined to only 9% of the saturation photocurrent.

In search for a deeper insight and realization of the physical origin of the aforementioned reduction and oxidation peaks in the region of -0.4 to 1.4 V, cyclic voltammetry experiments were carried out by varying the lower and upper limits of the scan under illumination (Fig. 5a). As shown in Fig. 5a the reduction cathodic peak at 0.2 V is directly related to the oxidic species that are accumulated on the illuminated TiO₂ surface at positive potentials higher than 0.4 V. The variation of the anodic limit of the voltammograms toward lower voltages results in the decrease of the reduction peak and in a shift of the peak to more positive potential (Fig. 5a). It completely disappears when the upper limit is set at 0.3 V. Interestingly the size of the anodic oxidation peak at 0.2 V is affected too, accompanied by a decrease in the peak voltage by 0.06 V. However, no effect is detected in the anodic oxidation peak positioned at -0.15 V.

As it is clearly depicted in Fig. 5b, the two oxidation peaks during the anodic scan are severely affected when the negative limit of the cyclic voltammogram is shifted toward positive potentials. The anodic peak located around 0.2 V is completely eliminated when the cathodic scan limit is positioned at 0 V. These results show that the cathodic reduction and anodic oxidation peaks at 0.1 V and 0.2 V respectively do not correspond to the same redox reaction. In addition the two anodic oxidation peaks reveal the existence of two redox processes involved in the reduction and oxidation of the TiO₂ surface.

3.3. Potentiostatic measurements

Fig. 6a depicts steady state potentiostatic measurements for different film thicknesses. The variation of the film thickness affects significantly both the photoelectrokinetics and the OCV of the TiO₂ photoelectrodes. As it is shown a three-fold increase in the saturation photocurrent is observed with an increase of the film thickness by 50% only. Note that its value is reached at more positive electrode voltages. In the case of the thicker photoelectrode saturation current is obtained even at more positive potential approaching 800 mV. Two of the most interesting observations depicted in Fig. 6a are: (i) the dependence of the OCV on the film thickness, and (ii) the existence of two distinct kinetic regions. In the case of the thin film electrode ($3.27 \mu\text{m}$, sample A) the OCV, upon irradiation, is at 0.2 V vs. RHE, while in the case of the other two thicker electrodes shown in Fig. 6a the OCV values obtained are positioned at -0.05 V and -0.08 V vs. RHE respectively. Initially a

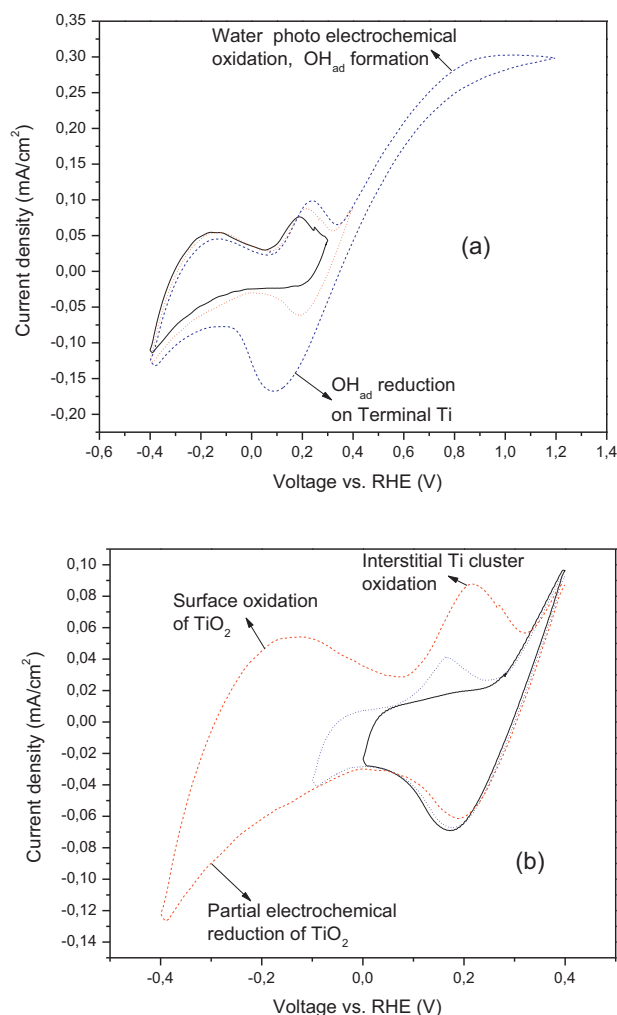


Fig. 5. Variation of cyclic voltammogram limits. Variation of the positive limit (a) and negative limit (b). Scan rate 5 mV/s. Sample B see Table 1.

linear variation of the photocurrent (kinetic region I) is observed up to a certain threshold, which depends on the film thickness and lies between 0.2 and 0.4 V. Thereafter a significant increase in the slope of the photocurrent vs. applied voltage is observed (kinetic region II), which ends to the plateau value of the saturation photocurrent (region III). The evident change of the slope from region I to region II indicates significant variation on the photo electrokinetic mechanism that drives the photocurrent evolution.

The efficiency of the water splitting process for the data depicted in Fig. 6a is shown in Fig. 6b and it is calculated according to Eq. (6). It represents the percentage of the incident electromagnetic energy that is being stored as chemical energy in H₂ taking into account the expense of electrochemical energy supply due to the application of the positive bias potential. A maximum in the efficiency is obtained upon approaching the saturation photocurrent i.e. on the border of regions II and III. The maximum value achieved depends on nanoparticulate TiO₂ film thickness. The losses in light conversion into H₂ at maximum efficiency as calculated by Eq. (6) (due to the applied bias potential) vary between 25 and 50%. As it will be further discussed, the losses can be either due to recombination kinetics as this can be the case of the slow reaction in region I of Fig. 6a or due to electron diffusion limitations across the nanoparticulate TiO₂ film.

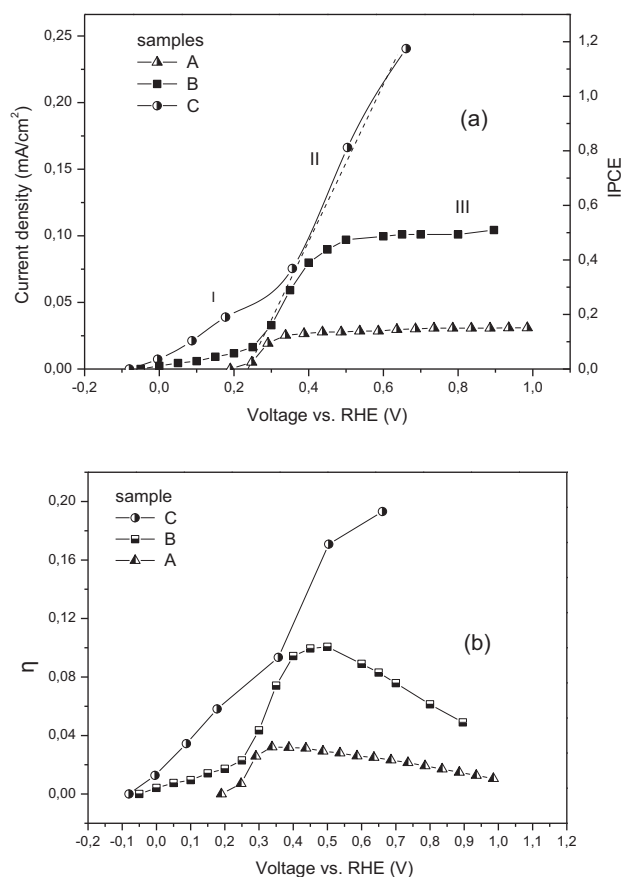


Fig. 6. Steady state potentiostatic plots of samples with varying film thickness. (a) 'Current density–Voltage' (I – V) and 'IPCE–Voltage' (IPCE– V) plots for various samples. (b) 'Efficiency–Voltage', (η – V). Efficiency is calculated according to Eq. (6), $\eta = \Delta G^\circ r_p - V_{\text{bias}} i_p / P_T$. Samples A, B and C are described in Table 1.

3.4. Oxygen evolution

For the case of sample C the evolved O_2 along the I – V curve was measured by means of online gas chromatography. The measured photocurrent and O_2 evolution rate expressed as faradaic current are plotted versus the applied voltage in Fig. 7. As far as we know, oxygen evolution is detected for the first time either through a photo electrochemical or a photocatalytic process. It is

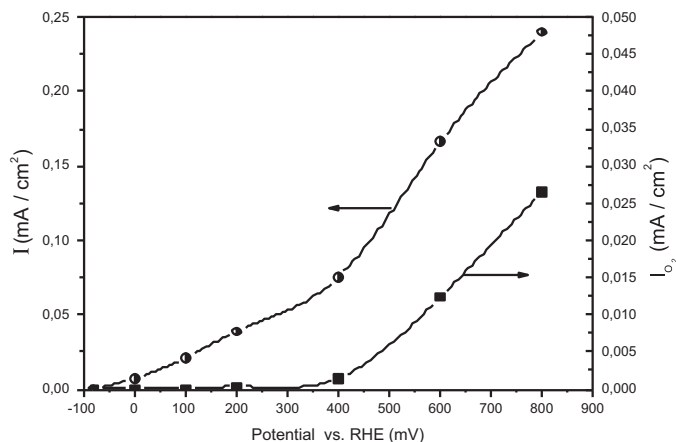


Fig. 7. Steady state 'current density (I) and O_2 evolution rate (I_{O_2}) vs Voltage' plots. I_{O_2} is calculated from Faraday's law based on on-line GC analysis. Sample C see Table 1.

evident that O_2 evolution essentially appears above 0.3 V, thus coinciding with the onset of region II photocurrent in the positive bias potential region. Only a portion of the photocurrent corresponds to oxygen evolution. O_2 selectivity (faradaic efficiency) increases with increasing current and voltage and reaches 10% at 0.8 V and $I = 0.24 \text{ mA/cm}^2$. The very low O_2 faradaic selectivity rather implies that O_2 production is concomitant to the anodic production of H_2O_2 .

4. Discussion

4.1. H_2O splitting on TiO_2 active sites

The kinetic interaction of H_2 with the illuminated TiO_2 photoanode is depicted in Fig. 4. As it is clearly shown, H_2 is reacting with the adsorbed oxidic species on TiO_2 , as this is evidenced by the elimination of the reduction cathodic peak at 0.06 V during H_2 bubbling. Nevertheless its contribution to the increase in photocurrent, as compared to the case of He flow, is minimal. As long as H_2 reacts with the adsorbed OH_{ad} species we would expect that at positive applied voltage H_2 would react electrochemically with OH^- to higher oxidation currents. The minimal enhancement in the photo current implies that neither H_2 is adsorbed on the surface in order to react electrochemically with the OH^- , nor does the OH^- with the TiO_2 surface, so that it will react with the gas phase H_2 . On the contrary the shape of the CVs within the photo current region in Fig. 4, above 0.4 V, is insensitive to gas phase conditions and exhibit minimal hysteresis phenomena. Note that hysteresis phenomena are characteristic of charge transfer electrochemical reactions and electrochemically formed surface species, as it is the case depicted by the CVs of Fig. 5a and b at voltages negative of 0.4 V. The variation of the coverage of the adsorbed and electrochemically reacting species with varying electrode voltage would induce different electrokinetic behavior during the anodic and cathodic scan. The lack of hysteresis implies that a quantum process controls the photocurrent and is mainly dictated by the electrons' photoexcitation rate. The small increase in saturation photocurrent under H_2 bubbling conditions can be attributed to suppressed exciton recombination rate induced by the depletion of OH_{ad} species upon their reaction with H_2 .

In the present study we are proposing and discussing the idea that the photo activated species can be realized through the filling of the 'wet electron' orbitals with photoexcited electrons. This may cause the destabilization of the H bond, thus facilitating the release of H^+ in the solution according to reaction (7).



In an alkaline solution the protons H^+ will readily react with the hydroxyl ions OH^- to form H_2O (reaction (8)).



In addition, the 'wet electron's' short measured lifetime (15 fs) [25] was interpreted by considering its resonant charge transfer to the conduction band of TiO_2 . In this respect it can be assumed that the electron is not trapped but instead its fast relaxation may contribute to the fast electron diffusion/drift through the TiO_2 crystal. The above described process is schematically shown in Fig. 8. The configuration of the 'wet electron' orbitals incorporates the interaction of a dangling H on top of O_{br} and two H atoms from adsorbed H_2O molecules and is based on the model proposed by Onda et al. [9].

The destabilization of the H-bond of adsorbed water molecules by the photo activation of electrons from defect states to the 'wet electron' state, thus inducing the release of H^+ in the solution, which will thereafter react with the OH^- in the solution to produce water

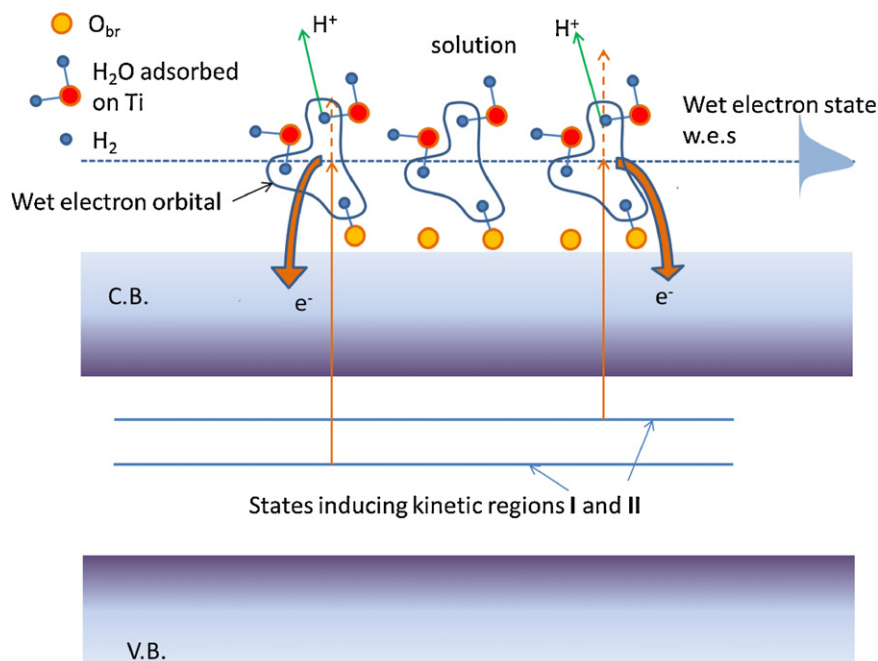


Fig. 8. Schematic representation of the photo electrochemical activation of the “wet electron” state. The configuration of the “wet electron” orbitals is based on the model proposed by Onda et al. [9] for water and OH_{ad} coverages 1 and 0.5 respectively. Each hydration cluster/orbital incorporates the interaction of a dangling H on top of O_{br} and two H atoms from adsorbed H_2O molecules. Electrons excitation from the two different band gap states induce different OCV values and are responsible for the appearance of kinetic regions I and II in Fig. 6.

(reactions (7) and (8)), fulfills the aforementioned considerations. Thereafter we can assume that the formed OH_{ad} species will react catalytically to form either H_2O_2 or O_2 (reactions (9) and (10)).



Taking into consideration that the ‘wet electron’ state is positioned 2.4 eV above the Fermi level of the defect states [25], which are localized within the band gap of TiO_2 , it is deduced that even with UV excitation at 365 nm (3.3 eV), the ‘wet electron’ state can be filled by electrons excited only by the defect states. These defect states can be formed during the heat treatment and/or negative potential scan of the nanocrystalline TiO_2 film and are positioned below the bottom of the conduction band. It is worth noticing that a perfect TiO_2 crystal without bulk or surface defect sites is not active for the photoelectrochemical water splitting either due to the limited surface adsorption capacity or due to the low quantum yield [26], even when irradiated with UV at 3.3 eV. Thus it is expected that the density of the bulk defect states below the bottom of the conduction band dictates the n-type semiconducting character of TiO_2 and its ability to act effectively as photoelectrode. Consequently the photon energy must be at least high enough so that an electron will be excited from the Fermi level to the ‘wet electron’ state. Based on theoretical calculations, Onda et al. [9] concluded that the energy level of the ‘wet electron’ state depends on the coverages of adsorbed water and the dangling H species on top of the bridged O_{br} and is located between 1.5 and 4.5 eV above the Fermi level. It must be noted that Onda et al. [9], as most of the researchers who investigate TiO_2 from a theoretical or a material science point of view, conducted their studies on rutile since it is considered more stable, while most of the applied/experimental work is done on anatase that is generally accepted as more efficient photo(electro)catalyst. According to Salvador [18] both anatase and rutile surfaces have 5-fold coordinated terminal Ti atoms, while a large part of terminal oxygen atoms (bridging oxygen ions) are 2-fold coordinated. Zhao et al. [27] in order to explain the differences in TPD measurements

between anatase and rutile argued that anatase interacts not only with the first monolayer of adsorbed H_2O (as rutile does), but also with the second forming loose H-bonds with dangling H-atoms. In [28] the authors discussed that the ‘wet electron’ orbitals are mostly distributed over a network of dangling H atoms. The H atoms that form the weakest H bonds receive the largest orbital density. From the above we can safely conclude that the existence and the role of the “wet electron” state should be more intense on anatase surface.

4.2. Electrode's efficiency and the electrochemical interface

Based on the CVs of Fig. 4 the OH_{ad} uptake was found 0.9×10^{15} species/cm² as this has been estimated by integrating the reduction peak at 0.1 V in Fig. 4 (sample B). We consider that the reacting OH_{ad} species adsorb on terminal pentacoordinated Ti sites, and the OH_{ad} uptake can be used for the determination and titration of the Ti surface species that are electrochemically active and participate in the photo electrochemical process. As has been mentioned we may safely argue that the coverage of 0.9×10^{15} species/cm² corresponds to 100% uptake of the anatase surface [10]. Thus, we can consider that full coverage of OH_{ad} on the TiO_2 electrode film surface is established, implying a fully extended electrochemical interface all over the nanoporous and nanoparticulate TiO_2 film, which is 100% photo electrochemically active. Consequently the turn over frequency for the H^+ production at the saturation photocurrent I_{sph} (region III of sample B), defined as $\text{TOF} = I_{\text{sph}} N_{\text{A}} / (F \cdot 0.9 \times 10^{15})$, is 0.7 s^{-1} . Thus considering that the IPCE value is <1 and increases with increasing thickness (Fig. 6a) it can be concluded that the incident radiation effectively penetrates through the bulk of the film thickness. In this respect the aforementioned value corresponds to the maximum TOF and must be independent of the intensity of the incident radiation. As it will be further discussed incident irradiation absorption rather depends on the limited number of the defect states within the bandgap of the TiO_2 nanocrystalline particles. The saturation photocurrent is therefore dictated by the extent of the electrochemical interface

and the electrocatalyst's amount as well as the specific surface area of the TiO_2 film. These parameters define the absolute population of the defect states within the TiO_2 nanocrystalline film. Thus an increase in the thickness of the TiO_2 film is expected to result into the linear increase of the saturation photocurrent if the photons penetrate through out the film. The optimum thickness of the photo electrode for a given incident irradiation power density can be defined by the threshold at which the IPCE value approaches unity in region III and the turn over frequency, based on the TiO_2 film's specific surface area, decreases to values below 0.7 s^{-1} . The latter is considered to be the maximum turn over frequency for the specific nanoparticulate photo electrodes with 100% photo electrochemically active specific surface area i.e. fully wetted and thoroughly illuminated. For the case of the $15 \mu\text{m}$ thick photoelectrode (sample C) the saturation photocurrent is solely determined by the flux intensity of the incident photons, as the IPCE appears to exceed 1 at the saturation photocurrent. This implies that all incident photons are being absorbed by the thick film of sample C. A solid and evident conclusion cannot be proposed at this stage for sample's C IPCE value >1 (Fig. 6a).

4.3. The role of the defect states in TiO_2 photo electrocatalysis

One of the biggest challenges regarding photoelectrocatalysis on TiO_2 is the understanding of the role of the surface structure and the functionality of the various active sites during the course of the photoelectrochemical water splitting. According to a general consensus the catalytic and photoelectrocatalytic properties of TiO_2 can be attributed to the defect sites of the crystal structure either at the surface or in the bulk of the material. It is already well established that these are located at the oxygen bridged (O_{br}) vacancies on the surface or at the Ti interstitial sites in the bulk [14,29–31]. According to Minato et al. [32] one O_{br} vacancy or OH impurity can change the charge distribution of more than 10 terminal Ti atoms, hence promoting the adsorption of electron accepting molecules on the Ti pentacoordinated terminal atoms.

Wendt et al. [14] proposed that the interstitial Ti located in the near surface region is mainly responsible for the defect states in the band gap and provides the electronic charge to the surface pentacoordinated Ti atoms, thus largely dictating their surface chemistry and specifically their intimate interaction with O, OH, H_2O and organic molecules. The interstitial Ti exists in the bulk even on a perfect defect-free surface and diffuses to the surface at elevated temperatures up to 400 K to react with O species and form TiO_x islands. Reversibly the various defects can be created by the removal of surface O_{br} species, hence inducing the diffusion of Ti species from the surface to the bulk as this was initially clarified by Henderson [29] by means of Temperature Program SIMS isotopic experiments. Several studies based on nuclear reaction analysis (NRA) [33], nuclear magnetic resonance (NMR) spin relaxation during diffusion of ^{49}Ti [34], radiotracer studies of ^{44}Ti diffusion [35] and ^{18}O depth profiling with SIMS [36,37] have reached to the common conclusion that the diffusion of Ti interstitials occurs orders of magnitude faster than oxygen diffusion. Iddir et al. [38] using the ab initio pseudopotential total-energy method concluded that Ti interstitials is the major diffusive species, since its low migration barrier is significantly smaller by 1 eV compared to that of O vacancies. As has been recently confirmed by Wendt et al. [14] by means of DFT calculations the diffusivity of Ti is energetically the most favorable pathway. Onda et al. [26] used two-photon photoemission spectroscopy and measured a significant decrease of the rutile TiO_2 work function upon the creation of defect states on a TiO_2 perfect surface by annealing, Ar^+ sputtering, and electron irradiation. The electron irradiation was causing the smaller decrease in the work function by the removal only of the surface O_{br} species. In the case of annealing and Ar^+ sputtering the work function was lower

and thus the Fermi level moves to higher energy levels closer to the bottom of the conduction band. This indicates that defect sites are created in the bulk with increased density of states within the band gap. These defect sites could not be healed by the exposure of the surface in oxygen as was the case of the electron irradiated surface. In this respect it can be considered that the bulk defect sites have a rather permanent character and play the main role both on the photoexcitation and on chemisorption/catalytic properties of the TiO_2 surface.

The chemisorptive properties of the terminal Ti atoms are largely dictated by the degree of TiO_2 reduction and specifically on the density of defect states that are created within the bandgap of TiO_2 [14]. As it is explicitly proposed by Wendt et al. [14] these bandgap states are substantiated through the existence of Ti interstitials in the near surface region and consist the main charge source to the terminal pentacoordinated Ti species. These states were detected at a position located 2 eV above the valence band maximum. Onda et al. [26] measured a maximum decrease in the work function 1.7 eV with respect to the perfect crystal surface, thus positioning the Fermi level of the defect states around 1.7 eV above the valence band maximum. It must be noted that the dissociative adsorption of O_2 on the surface of a perfect TiO_2 crystal (i.e. free of surface and bulk defects) is minimal due to the depletion of electronic charge on the terminal Ti electron donor sites [14]. This is corroborated by the fact of the substantially higher work function [9] and thus the deficient electron affinity as compared to the case where the defect states within the band gap can provide the electronic charge to the terminal Ti surface sites. The near surface defects, are creating electronic states within the band gap close to the bottom of the conduction band and seem to play a significant role in the photoexcitation properties of TiO_2 . It is reasonably expected that the density of these states will improve the photo excitation and photo reaction kinetics and will shift the light absorption to even lower energy. This was proven by the recent contribution from Chen et al. [8] who prepared black hydrogenated TiO_2 nanocrystals. They demonstrated a conceptually different approach to enhancing solar absorption by introducing disorder in the surface layers of nanocrystalline TiO_2 through hydrogenation at 20 bars and 200°C for 5 days. They have observed a broadened tail of states, from the valence band but also from the conduction band, extending into the band gap, resulting in the decrease of the band gap.

The transient behavior of the cyclic voltammograms depicted in Fig. 3a can be interpreted in the light of the aforementioned considerations. The progressive enhancement of the saturation photocurrent along the successive cyclic voltammograms can be attributed to the electrochemical reduction of the TiO_2 nanocrystalline electrode film at voltages more negative than -0.15 V , most probably resulting in the formation of defect sites within the bandgap. It must be noted that a cleaning surface procedure that can result in the increase of the electrochemical surface area along the successive cycles is excluded due to the non-varying reduction peak at 0.1 V of the adsorbed OH_{ad} species on the Ti terminal atoms. Therefore the increase in the saturation photocurrent can be sought in the enhanced absorption of the incident radiation through the successive cycles. This can be realized through the increased density of the defect states within the bandgap, which can be formed by the reduction of TiO_2 along the cathodic scan and specifically at electrode potentials more negative than -0.15 V . The reduction of TiO_2 occurs through the removal of surface O_{br} species and the diffusion of surface excess Ti^{3+} cations in the bulk of the nanoparticles, thus resulting in the formation of underlying near surface region interstitial Ti species [10,29]. Note that in the case of the cyclic voltammograms depicted in Fig. 3b the saturation photocurrent does not exceed 0.13 mA/cm^2 which is by a factor of 2 lower than the corresponding photocurrent of the cyclic voltammograms of

Fig. 3a (0.3 mA/cm^2). This significant difference can be attributed to the less negative value of the cathodic limit (-0.2 V) in the CVs of Fig. 3b. Therefore the TiO_2 electrode does not enter in the extended, up to -0.4 V , cathodic reduction region, in order to induce the formation of defect states either on the surface or in the bulk. It must be noted that in the case of the CVs of Fig. 3b both due to the less negative cathodic limit and the high voltage scan rate the negative current reduction part of the CV at voltages lower than 0.25 V corresponds only to the reduction of the adsorbed OH_{ad} species. Due to the high scan rate (50 mV/s) the peak resolution is very low.

The two anodic peaks at -0.15 V and 0.2 V (Fig. 2a) can be attributed to the reoxidation of the TiO_2 surface. As has been shown in Fig. 5a the two anodic peaks are not related with the reduction of the OH_{ad} species, which has been shown to be depleted from the electrode surface through the reduction process represented by the cathodic peak at 0.1 V . Instead these peaks must be related with the reoxidation of oxygen vacancies that had been created by scanning the potential to values negative of -0.15 V . It must be noted that the magnitude of the oxidation peak at 0.2 V depends somehow on the history of the sample and it increases with sample aging (Fig. 2b). Based on the previous discussion the enhancement of the oxidation peak at 0.2 V can be rationally attributed to the incremental accumulation of interstitial Ti species on the surface upon long-term exposure of the TiO_2 film in oxidative conditions [3]. Note that the OH_{ad} reduction peak at 0.1 V has been enhanced too, thus implying that the roughness factor of the nanocrystalline particle's surface has been increased. This is reasonably expected upon the development of the interstitial TiO_x clusters. Park et al. [39] studied their oxidation and reduction features by means of STM and DFT calculations and noticed a different reactivity as compared to the redox cycles of the supporting (110) rutile surface. This corroborates with the different oxidation potential (0.2 V) as compared to the more negative oxidation peak potential (-0.2 V) of the substrate TiO_2 surface (Fig. 5a). It is worth noticing that the oxidation peak at 0.2 V is being enhanced under illumination conditions (Fig. 2a). In addition the magnitude of the peak is negatively affected by the shift of the positive limit of the CVs of Fig. 5a toward lower positive values. Such behavior is in accord with the fast diffusion of the near surface underlying Ti interstitials onto the nanocrystalline particle's surface following the coverage of the OH_{ad} species. As has already been discussed this is in accordance to the well established knowledge in the literature that Ti interstitials appear and create clusters of TiO_x on the surface under oxidative conditions and high oxygen coverage [29]. This fast adjustment of the surface chemical structure either under illumination and/or applied potential can be the reason of the observed amphiphilic or oleophilic properties of the microstructured TiO_2 films [39].

4.4. Steady state photo-electro-kinetic behavior

The two kinetic regions I and II depicted in the potentiostatic experiment of Fig. 6a can be related rather to different bandgap states, as this is schematically depicted in Fig. 8. Their position in the bandgap and their recombination kinetics define both the open circuit voltage (OCV) and the slope of the photocurrent versus voltage. The shift of the OCV to more negative values can be attributed to excitons that absorb larger amount of the incident photons' energy. These originate from states that are positioned deeper in the bandgap and closer to the valence band maximum. However their low density can be the reason of the faster recombination rate. The distribution and the density of the various bandgap states depend on the degree of TiO_2 reduction [9,36]. Thus for example the irradiation of the surface with electrons induces a mild surface reduction

creating surface defects by the removal of bridged O_{br} species. These bandgap states are characterized by higher work function and they are positioned closer to the valence band maximum [9].

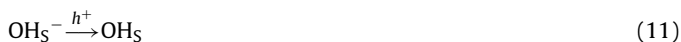
It is quite interesting to notice that both open circuit voltage and the slope of region I depend on the thickness of the TiO_2 film. Such behavior may be related to the increase of the absolute number of these bandgap states with increasing TiO_2 film thickness in relation to its interaction with the conducting substrate. The charge transfer from the conducting substrate to the TiO_2 film can rationalize the deactivation of these states in the case of thin TiO_2 films below $3 \mu\text{m}$ thick. Therefore, in the case of thin films, electrons from the substrate that may flow in order to equilibrate the Fermi levels at the substrate/film interface can spread within the whole mass of the film affecting the recombination kinetics of the excited states responsible for the appearance of region I. On the contrary in the case of thick films only a small portion of the film located close enough to the substrate/film interface can be affected [40].

Another reason for the losses along the I - V curves of the potentiostatic experiments of Fig. 6a can be attributed to the electron diffusion limitations across the nanoparticulate TiO_2 film, which causes significant ohmic losses at higher current densities and the shift of the saturation photocurrent to higher bias potential [8,41–43] (Fig. 6a). It is interesting to notice that the photocurrent in region II (Fig. 6a) lies on the same straight line for all TiO_2 films regardless of film thicknesses. Such behavior strongly indicates that the main parameter that determines photocurrent value is the majority charge carrier drift and diffusion across the film thickness on its way to the back contact current collector. These limitations are imposed by the grain boundaries resistance between the nanoparticles and the electron traps. The transfer of the photogenerated holes to the electrochemical interface is very fast in nano particle photoanode films with particle size less than 50 nm because the width of the space charge region is comparable to the particle's diameter with negligible band bending [41]. This is facilitated because of the porous structure of the films with highly developed surface area (high roughness factor = 200 – 1250) composed of nanocrystalline particles as low as 20 – 30 nm . In this respect it is possible to obtain a highly developed electrochemical interface on which the charge transfer electrochemical reactions can take place. The porosity ensures the wettability of the semiconductor's film all the way to the back contact. The 20 nm wetted nanoparticles will result in an interface with actually no band bending [41]. Hence, an effective charge separation can be extended throughout the bulk of the photoanode. It has been calculated that the voltage difference between the surface and the interior of a TiO_2 nanoparticle of 30 nm size is about 0.3 mV and can be considered as negligible [44].

The value of the open circuit potential is dictated by the oxidic species equilibrium coverage established on the illuminated TiO_2 surface in direct relation to the reduction potential. Taking into consideration that the flat band potential and open circuit electrode voltage are determined by the position of the Fermi level, two competing processes can be considered to contribute to the determination of the position of the Fermi level of the irradiated sample: (i) the injection of the electrons upon illumination to the conduction band and (ii) the surface adsorbed oxidic species, which act as electron acceptors and induce a decrease in the Fermi level.

The aforementioned competing process represent the hole trapping and recombination procedure, which was described kinetically by Salvador [45] in terms of the formation/accumulation on the surface of hydroxyl radicals (OH_5^\bullet) in comparison to the rate of formation of H_2O_2 . This is shown by the reactions (11) and (12) where adsorbed hydroxyl species (OH_5^-) react with holes (hole trapping) to produce OH_5^\bullet (reaction (9)) which subsequently

according to reaction (10) leads into the formation of adsorbed $\text{H}_2\text{O}_{2(s)}$.



Thereafter, as it is claimed [46,47], $\text{H}_2\text{O}_{2(s)}$ can react with holes for the production of O_2 . Recently H_2O_2 was massively detected both on the catalyst and in the solution during the photocatalytic water splitting and photo-electro reforming of glycerol [48] for H_2 production.

As it is evidently shown in Fig. 7 the majority of the photocurrent should correspond to the formation of H_2O_2 which is diluted in the solution. In fact the most stable electrochemical formation of H_2O_2 through the cathodic electro reduction of O_2 is processed in alkaline solution [49,50]. The final product is the formation of alkaline solutions containing H_2O_2 in the form of peroxide ions HO_2^- . Similarly, in the present study, the presence of high pH alkaline solution is assumed that results in the stabilization of the H_2O_2 formation. According to the previous discussion, we came to the conclusion that the photo electrochemical splitting of H_2O proceeds through the 'wet electron' mechanism of adsorbed H_2O molecules in the absence of anodic charge transfer reaction between the OH^- species and the TiO_2 surface. Thus the resulting adsorbed OH_{ad} species, formed through reaction (7), will react catalytically for the H_2O_2 formation according to reaction (9). Sequentially H_2O_2 may decompose to form O_2 and H_2O (reaction (10)). Most probably the low faradaic efficiency toward O_2 production can be attributed to the higher stability of H_2O_2 in the alkaline solution.

5. Conclusions

The present study highlights the contribution of the defect states within the TiO_2 bandgap and the activation of the 'wet electron' state for the photoelectrocatalytic water splitting. The mild electrochemical reduction of the TiO_2 photoelectrode enhances the n-type semiconducting character of TiO_2 by the formation of defect states within the bandgap closer to the conduction band. This results in a 2-fold enhancement of the photo electrochemical activity of the TiO_2 photoelectrode. The distinct variation of the energy levels of the defect states can be responsible for the two electrokinetic regions observed along the potentiostatic variation of the photocurrent with increasing photoelectrode's potential. The photoelectrokinetics of water splitting can be realized through the activation of the 'wet electron' state of the adsorbed water molecules, which may originate only from photoexcited electrons initially positioned on energy levels located within the bandgap and at least 2 eV above the valence band maximum and 2.4 eV below the 'wet electron' state. Thus the photons energy must be at least 2.4 eV.

References

- [1] M.G. Walter, E.L. Warren, J.R. McKone, S.W. Boettcher, Q. Mi, E.A. Santori, N.S. Lewis, *Chemical Reviews* 110 (2010) 6446–6473.
- [2] B.A. Gregg, *Journal of Physical Chemistry B* 107 (2003) 4688–4698.
- [3] A. Valdes, J. Brillet, M. Gratzel, H. Gudmundsdottir, H.A. Hansen, H. Jonsson, P. Klupfel, G.-J. Kroes, F. Le Formal, I.C. Man, R.S. Martins, J.K. Nørskov, J. Rossmeisl, K. Sivula, A. Vojvodic, M. Zach, *Physical Chemistry Chemical Physics* 14 (2012) 49–70.
- [4] J.H. Park, J.H. Noh, B.S. Han, S.S. Shin, I.J. Park, D.H. Kim, K.S. Hong, *Journal of Nanoscience and Nanotechnology* 12 (2012) 5091–5095.
- [5] D. Bari, A. Cester, N. Wrachien, L. Ciammaruchi, T.M. Brown, A. Reale, A. Di Carlo, G. Meneghesso, *IEEE Journal of Photovoltaics* 2 (2012) 27–34.
- [6] S. Palmas, A. Da Pozzo, M. Mascia, A. Vacca, P.C. Ricci, *Chemical Engineering Journal* 211–212 (2012) 285–292.
- [7] A.K. Seferlis, S.G. Neophytides, *ECS Transactions* 25 (42) (2010) 63–72.
- [8] X. Chen, L. Liu, P.Y. Yu, S.S. Mao, *Science* 331 (2011) 746–750.
- [9] K. Onda, B. Li, J. Zhao, K.D. Jordan, J. Yang, H. Petek, *Science* 308 (2005) 1154–1158.
- [10] M.A. Henderson, *Surface Science* 355 (1996) 151–166.
- [11] B. Li, J. Zhao, K. Onda, K.D. Jordan, J. Yang, H. Petek, *Science* 311 (2006) 1436–1440.
- [12] T.L. Villarreal, R. Gomez, M. Neumann-Spallart, N. Alonso-Vante, P. Salvador, *Journal of Physical Chemistry B* 108 (39) (2004) 15172–15181.
- [13] Y. Du, N.A. Deskins, Z. Zhang, Z. Dohnalek, M. Dupuis, I. Lyubintsev, *Physical Review Letters* 102 (2009) 096102–1–096102–4.
- [14] S. Wendt, P.T. Sprunger, E. Lira, G.K.H. Madsen, Z. Li, J.Ø. Hansen, J. Matthiesen, A. Blekinge-Rasmussen, E. Lægsgaard, B. Hammer, F. Besenbacher, *Science* 320 (2008) 1755–1759.
- [15] J. Matthiesen, J.Ø. Hansen, S. Wendt, E. Lira, R. Schaub, E. Lægsgaard, F. Besenbacher, B. Hammer, *Physical Review Letters* 102 (2009) 226101.
- [16] S. Wendt, J. Matthiesen, R. Schaub, E.K. Vestergaard, E. Lægsgaard, F. Besenbacher, B. Hammer, *Physical Review Letters* 96 (2006) 066107.
- [17] A. Imanishi, T. Okamura, N. Ohashi, R. Nakamura, Y. Nakato, *Journal of the American Chemical Society* 129 (2007) 11569–11578.
- [18] P. Salvador, *Progress in Surface Science* 86 (2011) 41–58.
- [19] Z. Zhang, Y. Du, N.G. Petrik, G.A. Kimmel, I. Lyubintsev, Z. Dohnalek, *Journal of Physical Chemistry C* 113 (2009) 1908–1916.
- [20] P. Bouras, E. Stathatos, P. Lianos, C. Tsakiroglou, *Applied Catalysis B: Environmental* 51 (4) (2004) 275–281.
- [21] A.K. Seferlis, S.G. Neophytides, *Journal of the Electrochemical Society* 158 (2) (2011) H183–H189.
- [22] O.K. Varghese, C.A. Grimes, *Solar Energy Materials & Solar Cells* 92 (2008) 374–384.
- [23] J. Georgieva, S. Armanyanov, E. Valova, I. Poulis, S. Sotiropoulos, *Electrochimica Acta* 51 (2006) 2076–2087.
- [24] Z. Zhao, Z. Li, Z. Zou, *Journal of Physics: Condensed Matter* 22 (2010) 175008.
- [25] K.D. Jordan, *Science* 306 (2004) 618–619.
- [26] K. Onda, B. Li, H. Petek, *Physical Review B* 70 (2004) 045415.
- [27] J. Zhao, B. Li, K. Onda, M. Feng, H. Petek, *Chemical Reviews* 106 (2006) 4402–4427.
- [28] J. Zhao, B. Li, K.D. Jordan, J. Yang, H. Petek, *Physical Review B* 73 (2006) 195309.
- [29] M.A. Henderson, *Surface Science* 419 (1999) 174–187.
- [30] P. Kruger, S. Bourgeois, B. Domenichini, H. Magnan, D. Chandesris, P. Le Fevre, A.M. Flank, J. Jupille, L. Floreano, A. Cossaro, A. Verdini, A. Morgante, *Physical Review Letters* 100 (2008) 055501.
- [31] Z. Li, J.Ø. Hansen, J. Matthiesen, A. Blekinge-Rasmussen, E. Lægsgaard, B. Hammer, F. Besenbacher, *Science* 320 (2008) 1755.
- [32] T. Minato, Y. Sainoo, Y. Kim, H.S. Kato, K. Aika, M. Kawai, J. Zhao, H. Petek, T. Huang, W. He, B. Wang, Z. Wang, Y. Zhao, J. Yang, J.G. Hou, *Journal of Chemical Physics* 130 (2009) 124502.
- [33] D.J. Derry, D.G. Lees, J.M. Calvert, *Journal of Physics and Chemistry of Solids* 42 (1981) 57–64.
- [34] H. Kolem, O. Kanert, *Zeitschrift für Metallkunde* 80 (1989) 227–234.
- [35] K. Hoshino, N.L. Peterson, C.L. Wiley, *Journal of Physics and Chemistry of Solids* 46 (1985) 1397–1411.
- [36] M. Arita, M. Hosoya, M. Kobayashi, M. Someno, *Journal of the American Ceramic Society* 62 (1979) 443–446.
- [37] M. Someno, M. Kobayashi, *Springer Series in Chemical Physics* 9 (1979) 222.
- [38] H. Iddir, S. Ögüt, P. Zapol, N.D. Browning, *Physical Review B* 75 (2007) 073203.
- [39] K.T. Park, M. Pan, V. Meunier, E.W. Plummer, *Physical Review B* 75 (2007) 245415.
- [40] R. Wang, K. Hashimoto, A. Fujishima, M. Chikuni, E. Kojima, A. Kitamura, M. Shimohigoshi, T. Watanabe, *Nature* 388 (1997) 431–432 (31 July).
- [41] S. Sodergren, A. Hagfeldt, J. Olsson, S.-E. Lindquist, *Journal of Physical Chemistry* 98 (1994) 5552–5556.
- [42] N. Kipidakis, E.A. Schiff, N.-G. Park, J. van de Lagemaat, A.J. Frank, *Journal of Physical Chemistry B* 104 (2000) 3930–3936.
- [43] L.M. Peter, D. Vanmaekelbergh, in: R.C. Alkire, D.M. Kolb (Eds.), *Advances in Electrochemical Science and Engineering*, WILEY-VCH Verlag GmbH, Weinheim, Germany, 1999, <http://dx.doi.org/10.1002/9783527616800.ch2>.
- [44] B. O'Regan, J. Moser, M. Anderson, M. Gratzel, *Journal of Physical Chemistry* 94 (1990) 8720–8726.
- [45] P. Salvador, *Journal of Physical Chemistry* 89 (1985) 3863–3869.
- [46] P. Salvador, F. Decker, *Journal of Physical Chemistry* 88 (1984) 6116–6120.
- [47] P. Salvador, C. Gutierrez, *Surface Science* 124 (1983) 398–406.
- [48] V.M. Daskalaki, P. Panagiotopoulou, D.I. Kondarides, *Chemical Engineering Journal* 170 (2011) 433–439.
- [49] K. Kinoshita, *Electrochemical Oxygen Technology*, John Wiley & Sons Inc., New York, 1992, p. 369.
- [50] E.L. Gyenge, C.W. Oloman, *Journal of the Electrochemical Society* 152 (3) (2005) D42–D53.